nature photonics

LETTERS

PUBLISHED ONLINE: 24 APRIL 2011 | DOI: 10.1038/NPHOTON.2011.51

Ultralow-threshold electrically pumped quantum-dot photonic-crystal nanocavity laser

Bryan Ellis[1], Marie A. Mayer[2,3], Gary Shambat[1], Tomas Sarmiento[1], James Harris[1], Eugene E. Haller[2,3] and Jelena Vučković[1]*

Efficient, low-threshold and compact semiconductor laser sources are under investigation for many applications in high-speed communications, information processing and optical interconnects. The best edge-emitting and vertical-cavity surface-emitting lasers have thresholds on the order of 100 μA (refs 1,2), but dissipate too much power to be practical for many applications, particularly optical interconnects[3]. Optically pumped photonic-crystal nanocavity lasers represent the state of the art in low-threshold lasers[4,5]; however, to be practical, techniques to electrically pump these structures must be developed. Here, we demonstrate a quantum-dot photonic-crystal nanocavity laser in gallium arsenide pumped by a lateral p–i–n junction formed by ion implantation. Continuous-wave lasing is observed at temperatures up to 150 K. Thresholds of only 181 nA at 50 K and 287 nA at 150 K are observed—the lowest thresholds ever observed in any type of electrically pumped laser.

Photonic-crystal nanocavities are an ideal platform for low-power laser sources, because a strong light–matter interaction can be achieved. High quality factors ($>1 \times 10^6$) have been demonstrated in cavities with mode volumes comparable to a cubic-optical wavelength[6,7]. In such cavities, the Purcell factor can be quite high, reducing the lasing threshold and increasing the modulation rate[8]. Optically pumped photonic-crystal nanocavity lasers have been demonstrated to have thresholds of only a few nanowatts[9] and modulation rates exceeding 100 GHz (ref. 10). In addition, they can operate in continuous-wave mode at room temperature[11] and can be efficiently coupled to low-loss waveguides for optoelectronic integrated circuit applications[12].

The principal disadvantage of photonic-crystal nanocavity lasers is that they are intrinsically difficult to electrically pump, because it is challenging to inject carriers through the membrane to the active region in an efficient manner. For this reason, all of the aforementioned demonstrations relied on impractical optical pumping. Lasing has been demonstrated in a photonic-crystal nanocavity by directing the current to the cavity region using a vertical p–i–n junction and a current post[13,14]. However, the current post limits the quality factor of the cavity, restricts the choice of cavity design, and requires a complicated fabrication procedure[14]. In addition, a high threshold current of 260 μA (corresponding to a power dissipation of 260 μW) was observed, which is significantly higher than in optically pumped photonic-crystal devices, even exceeding values achieved in vertical-cavity surface-emitting lasers (VCSELs)[2]. In this work we present a simpler and more flexible fabrication procedure that gives better control over current flow. This has enabled us to demonstrate a laser with threshold power dissipation comparable to that demonstrated in optically pumped photonic-crystal devices.

We demonstrate a photonic-crystal nanocavity laser that is electrically pumped by a lateral p–i–n junction (shown schematically in Fig. 1a)[15,16]. The intrinsic region is designed to be 400 nm wide in the cavity region, extending to a width of 5 μm to the sides of the cavity. This design efficiently directs the current flow through the cavity region. We chose a modified three-hole defect photonic-crystal cavity design[17]. Figure 1b shows a finite-difference time-domain (FDTD) simulation of the fundamental cavity mode, with a theoretically estimated quality factor of 115,000, which is comparable to previous studies of similar cavities[18].

Ion implantation of beryllium and silicon ions was used to dope the p- and n-type regions, respectively. Because implantation of high-energy ions causes some lattice damage that will lead to a reduction in gain, it is critical that the p and n regions are precisely aligned to the photonic-crystal cavity to avoid damaging the active region. We developed a fabrication procedure in which the ions were implanted through silicon nitride masks patterned by electron-beam lithography to achieve an alignment accuracy of ~30 nm (see Methods). The gain material for the laser comprised three layers of high-density (300 μm^{-2}) InAs quantum dots. To activate the ion-implanted dopants, we performed a high-temperature anneal. This anneal procedure was optimized (see Methods and Supplementary Information) to give sufficient dopant activation without significantly changing the emission properties of the

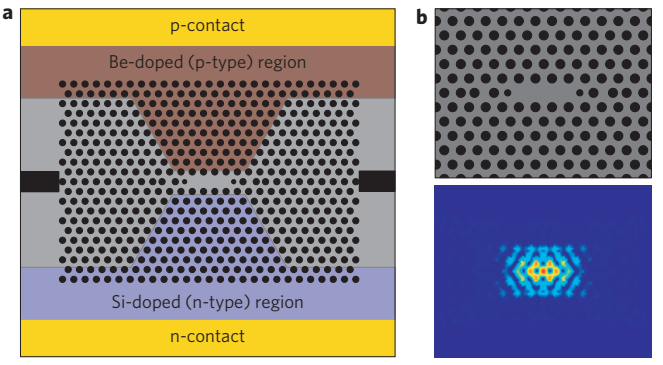

Figure 1 | Design of the electrically pumped photonic-crystal laser. **a**, Schematic of the electrically pumped photonic-crystal laser. The p-type doping region is indicated in red, and the n-type region in blue. The width of the intrinsic region is narrow in the cavity region to direct current flow to the active region of the laser. A trench is added to the sides of the cavity to reduce leakage current (see Methods). **b**, Modified three-hole defect photonic-crystal cavity design (top) and a FDTD simulation of the E-field of the cavity mode in such a structure (bottom).

[1]Department of Electrical Engineering, Stanford University, Stanford, California 94305, USA, [2]Materials Sciences Division, Lawrence Berkeley National Laboratory, Berkeley California 94720, USA, [3]Department of Materials Science, University of California, Berkeley, Berkeley, California 94720, USA.
*e-mail: jela@stanford.edu

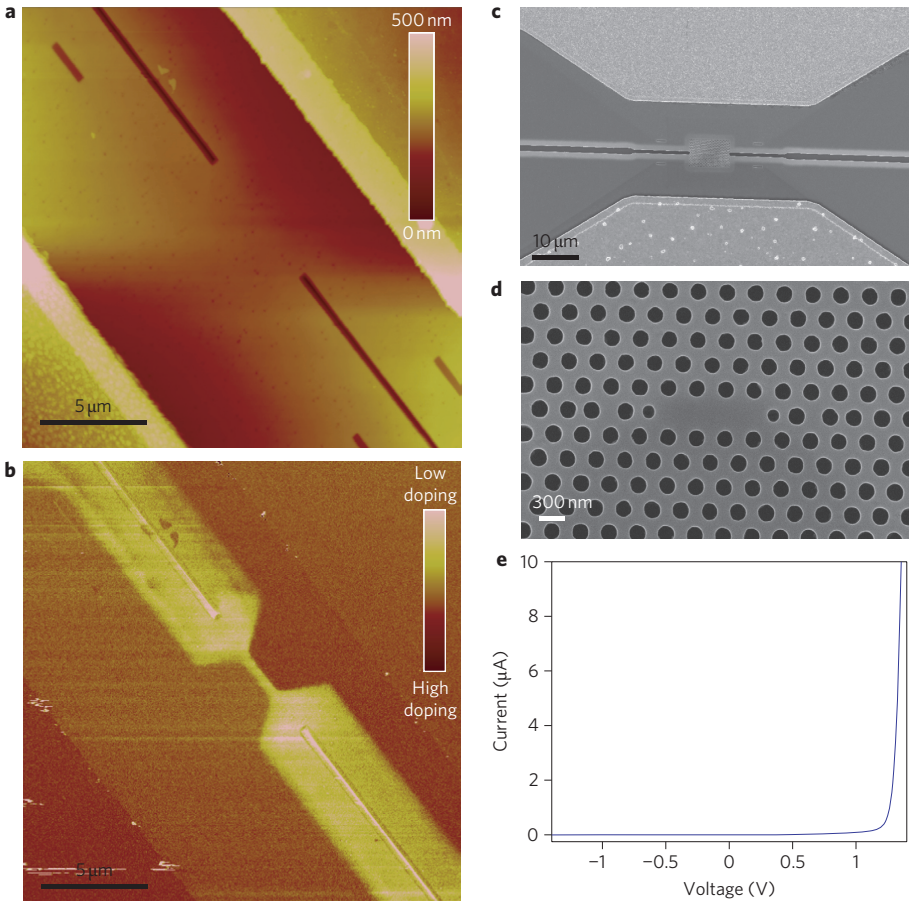

Figure 2 | Fabrication and characterization of the photonic-crystal laser device. a, AFM topography image of the fabricated device without photonic crystal. **b**, SCM image of the region in **a**. The p-side of the device is in the lower left corner and the n-side in the upper right. The trench is etched at the device centre, showing the precision of the alignment of the doping regions. 'SCM data' is a combination of the phase and amplitude of capacitance data, where the strength of the signal is directly proportional to the intensity of doping in the local region under the tip. **c**, SEM image of the fully fabricated laser. The p-side of the device appears on the top of the image, and the n-side on the bottom. **d**, SEM image of the photonic-crystal cavity (zoom-in of the central region of **c**). **e**, Current–voltage characteristics of the laser taken at 50 K in the dark.

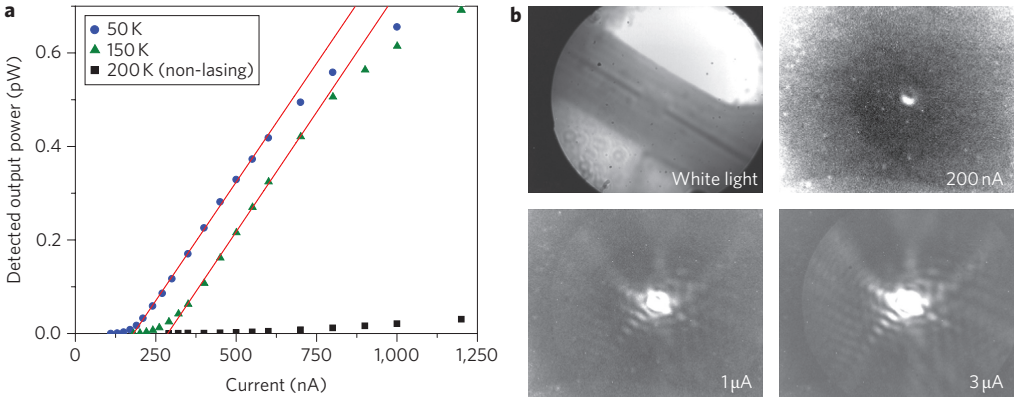

Figure 3 | Optical output of the photonic-crystal laser. a, Experimental output power (detected on the spectrometer) as a function of the current through the laser at 50 K (blue points), 150 K (green points) and 200 K (non-lasing; black points). Red lines are linear fits to the above threshold output power of the lasers, which are used to find the thresholds. We estimate from the collected output power that the total radiated power of the laser above threshold is on the order of a few nanowatts. **b**, Far-field radiation patterns of the laser at currents of 200 nA, 1 μA and 3 μA taken at 50 K. A white light image of the cavity is also shown. The n-contact is in the lower left corner of the image, and the p-contact in the upper right.

quantum dots. Following the activation anneal, we found that the peak photoluminescence wavelength of the quantum dots was 1,175 nm at 100 K. We found that the average doping densities in the membrane (after dopant activation) were 6.0×10^{17} cm^{-3} and 2.5×10^{19} cm^{-3} in the n and p regions, respectively (see Supplementary Information).

To confirm the doping layout before fabrication of the photonic-crystal cavity, we used atomic force microscopy (AFM) and scanning

capacitance microscopy (SCM)[19]. Figure 2a,b shows the AFM topography and SCM data for structures without photonic crystals, demonstrating that the desired dopant layout is achieved. From these data we can identify the exact locations of the doping regions and precisely position the photonic-crystal cavity in the centre of the intrinsic region (see Supplementary Information). Figure 2c,d shows scanning electron microscopy (SEM) images of the fabricated photonic-crystal laser. The parameters of the cavity were chosen so that the fundamental cavity mode was at a wavelength of 1,174 nm at low temperatures, within the ground-state emission of the quantum dots. We confirmed that this mode was the fundamental mode of the cavity by identifying the higher-order cavity modes in the electroluminescence spectra and comparing them with FDTD results. Figure 2e shows the current–voltage characteristics of the fabricated laser diode at 50 K.

Figure 3a presents the optical output power of the laser as a function of continuous-wave pump current at several different temperatures. A clear lasing threshold can be observed for temperatures below 150 K. As the temperature increases, the quantum-dot resonance wavelength and the cavity resonance wavelength redshift at different rates. At higher temperatures, the photonic-crystal cavity resonances are no longer within the gain bandwidth of the quantum dots. A measurement on the same structure at 200 K (at which no lasing is observed) is included for comparison. To determine the threshold of our laser we applied a linear fit to the above-threshold characteristics and extrapolated it to zero-output power (red lines in Fig. 3a). We found that the threshold of our laser was 181 nA at 50 K and 287 nA at 150 K. To the best of our knowledge, this is the lowest threshold ever demonstrated in an electrically pumped semiconductor laser. It is three orders of magnitude better than the 260 μA threshold demonstrated in quantum-well photonic-crystal cavity lasers[13] and more than an order of magnitude better than the thresholds demonstrated in metal-clad lasers[20] and micropost lasers[21]. The low thresholds demonstrated in these lasers can be attributed to better control over the current flow, and the reduced surface recombination in quantum-dot-based photonic-crystal lasers[22]. At threshold, the applied voltage is only 1.15 V at 50 K and 1.03 V at 150 K, meaning that at threshold the lasers consume only 208 nW at 50 K and 296 nW at 150 K. From the collected power, we can estimate the total power radiated by the laser to be on the order of a few nanowatts well above threshold[23] (see Supplementary Information). Figure 3b shows the experimental far-field radiation pattern of the cavity at various current levels.

The laser linewidth (full-width at half-maximum) as a function of current is plotted in Fig. 4a. The linewidth narrows from ~1.35 nm just below threshold to 0.95 nm well above threshold. The quality factor of the cavity mode at threshold is ~1,130. This quality factor is significantly smaller than expected from FDTD simulations, probably due to free carrier absorption or surface roughness introduced by the fabrication procedure. Room-temperature optically pumped lasing in nanocavities with similar quantum dots has recently been demonstrated[11,24], and we believe that further refinements to the fabrication procedure will allow us to demonstrate electrically pumped lasing at room temperature (see Supplementary Information).

Although we have optimized our device design to reduce leakage current (see Methods), at low voltages before the diode has fully turned on we observed leakage current bypassing the cavity through the sacrificial layer and substrate. Therefore, if the device design is further improved to reduce this leakage, the threshold could be significantly lower. To find the potential threshold reduction, we fit the current–voltage characteristics to an ideal diode equation to determine the fraction of current flowing through the cavity as a function of applied voltage (see Supplementary Information). The light output of the laser as a function of current after subtracting leakage is plotted in Fig. 4b (blue points), together with a fit to the laser rate

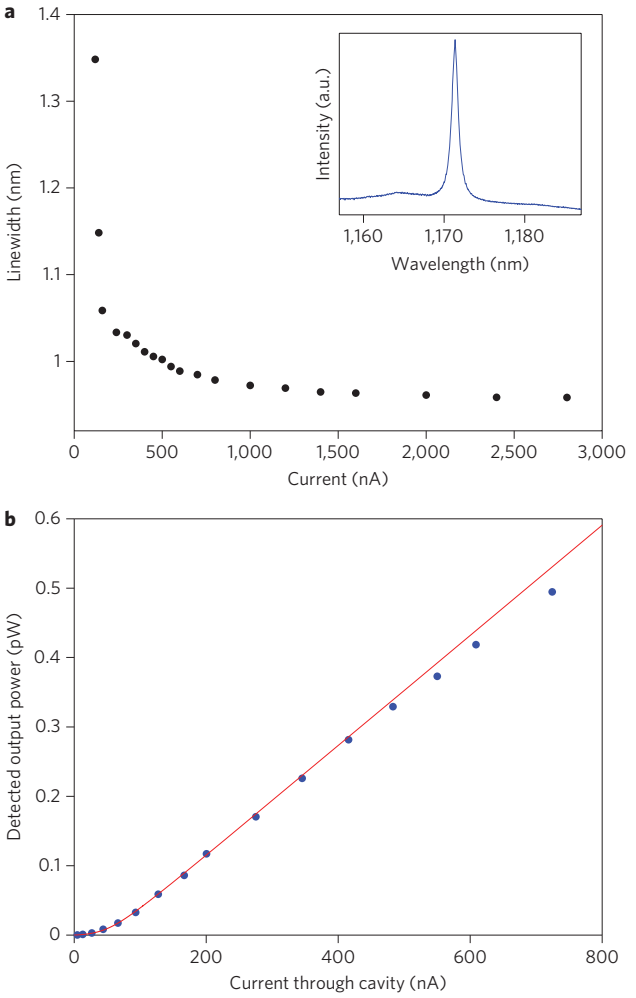

Figure 4 | Optical properties of the photonic-crystal laser. a, Linewidth of the photonic-crystal laser as a function of current. Inset: spectrum of the photonic-crystal laser at a pump current of 1 μA. **b**, This figure re-plots the data shown in Fig. 3a for 50 K after subtracting the leakage current of the diode (blue points); the result is then fitted to the laser rate equations (red line). 'Current through cavity' (on the horizontal axis) refers to the current flowing through the cavity region after subtracting leakage through the substrate (see text and Supplementary Information).

equations. From the fit and simulations of the Purcell factor in our cavity (see Supplementary Information), we determine that the fraction of spontaneous emission that is coupled to the cavity mode (commonly called the β-factor[8]) is between 0.29 and 0.41 in our laser. The laser threshold after correcting for the leakage current is only 70 nA.

In summary, we have designed and demonstrated an electrically pumped quantum-dot photonic-crystal nanocavity laser. The laser operates in continuous-wave mode at temperatures up to 150 K, and exhibits ultralow thresholds of 181 nA at 50 K and 287 nA at 150 K. If we subtract the leakage current flowing into the substrate, the threshold current is estimated to be ~70 nA. These lasing thresholds are three orders of magnitude lower than previous demonstrations of electrically pumped photonic-crystal nanocavity lasers, and lower than any electrically injected laser to date. We believe that room-temperature operation is possible if the quality factors of the cavity can be improved, and if the cavity resonances are better aligned to the quantum-dot gain spectrum at room temperature. In addition, it should be possible to integrate this laser on a silicon chip by wafer bonding techniques if the high-temperature steps are performed before bonding. The low-power dissipation of

these lasers makes them very promising for applications in optical interconnects and high-speed communications, as well as for fundamental studies of the properties of electrically pumped thresholdless lasers and lasers with single-emitter gain[25].

Methods

Wafer Growth. The wafer was grown using molecular beam epitaxy. Starting with a semi-insulating substrate, a 1 μm $Al_{0.95}Ga_{0.05}As$ sacrificial layer was grown, followed by a 220 nm GaAs membrane that contained three layers of InAs quantum dots separated by 50 nm GaAs spacers. The dots were formed by depositing 2.8 monolayers of InAs at 510 °C using a growth rate of 0.05 monolayers per second. The dots were capped with a 6 nm $In_{0.15}Ga_{0.85}As$ strain-reducing layer. The resulting dot density was ~300 dots per μm^2, as confirmed by AFM measurements of uncapped quantum-dot samples.

Fabrication. Alignment marks were defined on the unpatterned wafer using electron-beam lithography and dry-etched ~100 nm into the membrane using an $Ar/Cl_2/BCl_3$ electron-cyclotron resonance reactive ion etch (ECR-RIE). A 330 nm layer of silicon nitride was then deposited on the sample using plasma-enhanced chemical vapour deposition (PECVD) to serve as a mask for ion implantation of silicon. Electron-beam lithography was used to pattern the n-type doping region, and an SF_6/C_2F_6 dry etch was used to remove the nitride from the n-type doping area. Silicon ions were implanted with an energy of 115 keV and a dose of 3×10^{14} cm^{-2}. A SF_6/C_2F_6 dry etch was used to remove the remaining silicon nitride, and another 330 nm layer of silicon nitride was deposited on the sample using PECVD to serve as the mask for ion implantation of beryllium. Electron-beam lithography was used to pattern the p-type doping region and a SF_6/C_2F_6 dry etch was used to remove the silicon nitride from the p-type doping area. Beryllium ions were implanted with an energy of 32 keV and a dose of 2.5×10^{15} cm^{-2}. An SF_6/C_2F_6 dry etch was used to remove the remaining silicon nitride. A 40 nm tensile-strained silicon nitride cap was deposited using PECVD to prevent out-diffusion of arsenic during the subsequent high-temperature anneal. The samples were then annealed at 850 °C for 15 s in a rapid thermal annealer to activate the dopants and remove almost all of the lattice damage caused by ion implantation. A SF_6/C_2F_6 dry etch was used to remove the nitride cap. The photonic-crystal pattern was defined using electron-beam lithography and etched into the membrane using an $Ar/Cl_2/BCl_3$ ECR-RIE. Simultaneously with the photonic crystal, trenches were etched to the sides of the cavity and all the way around each of the contacts; this was found to reduce the leakage current to reasonable levels. Next, the photonic crystal was loaded into a wet thermal oxidation furnace and the sacrificial layer was oxidized at 465 °C for 7 min. Photolithography and electron-beam evaporation were used to define Au/Ge/Ni/Au n-type contacts in a lift-off process. Photolithography and sputtering were used to define Au/Zn/Au p-type contacts, also in a lift-off process. The contacts were then annealed at 415 °C for 15 s to achieve a minimum contact resistance. Finally, 45% potassium hydroxide solution in water was used to remove the oxidized sacrificial layer under the cavity, leaving an air-clad photonic-crystal membrane.

Sample characterization. The Hall effect was used to find the carrier sheet concentration in semi-insulating GaAs test samples implanted under the same conditions as the laser samples. The doping profile was measured using an electrochemical capacitance voltage measurement using 0.1 M NaOH with ethylenediaminetetraacetic acid (EDTA) surfactant as the electrolyte. An atomic force microscope with a scanning capacitance attachment was used to measure the doping layout on the actual laser samples on devices without photonic crystals. A two-plate-capacitor set-up for scanning consisted of the sample, native surface oxide and a gold-coated AFM tip used in contact mode with a scanning bias of 1 V.

Sample optical testing. The sample was epoxied to an alumina chip carrier using non-conductive, vacuum-safe epoxy. Aluminium wirebonds were used to connect individual devices to the leads of the chip carrier, and the chip carrier was loaded into a continuous-flow helium cryostat with custom-designed coldfinger and electrical feedthroughs. The temperature was stabilized to within 0.5 K. Currents were applied using a source meter with sub-nano-amp accuracy. The emission from the sample was collected using an objective lens with a numerical aperture of 0.5 in the direction perpendicular to the sample surface. Emission spectra were measured using a spectrometer with a liquid-nitrogen-cooled InGaAs charge-coupled device (CCD) detector, and luminescence images were taken with an InGaAs CCD camera.

Received 14 December 2010; accepted 17 March 2011; published online 24 April 2011

References

1. Lau, K. Y., Derry, P. L. & Yariv, A. Ultimate limit in low threshold quantum well GaAlAs semiconductor lasers. *Appl. Phys. Lett.* **52,** 88–90 (1988).
2. MacDougal, M. H., Dapkus, P. D., Pudikov, V., Zhao, H. & Yang, G. M. Ultralow threshold current vertical-cavity surface-emitting lasers with AlAs oxide-GaAs distributed Bragg reflectors. *IEEE Photon. Technol. Lett.* **7,** 229–231 (1995).
3. Miller, D. Device requirements for optical interconnects to silicon chips. *Proc. IEEE* **97,** 1166–1185 (2009).
4. Loncar, M., Yoshie, T., Scherer, A., Gogna, P. & Qiu, Y. Low threshold photonic crystal laser. *Appl. Phys. Lett.* **81,** 2680–2682 (2002).
5. Noda, S. Photonic crystal lasers — ultimate nanolasers and broad area coherent lasers. *J. Opt. Soc. Am. B* **27,** B1–B8 (2010).
6. Takahashi, Y. *et al.* High-*Q* nanocavity with a 2-ns photon lifetime. *Opt. Express* **15,** 17206–17213 (2007).
7. Tanabe, T., Notomi, M., Kuramochi, E., Shinya, A. & Taniyama, H. Trapping and delaying photons for one nanosecond in an ultrasmall high-*Q* photonic crystal nanocavity. *Nature Photon.* **1,** 49–52 (2007).
8. Bjork, G. & Yamamoto, Y. Analysis of semiconductor microcavity lasers using rate equations. *IEEE J. Quantum Electron.* **27,** 2386–2396 (1991).
9. Strauf, S. *et al.* Self-tuned quantum dot gain in photonic crystal lasers. *Phys. Rev. Lett.* **96,** 127404 (2006).
10. Altug, H., Englund, D. & Vuckovic, J. Ultrafast photonic crystal nanocavity laser. *Nature Phys.* **2,** 484–488 (2006).
11. Nomura, M. *et al.* Room temperature continuous-wave lasing in photonic crystal nancavity. *Opt. Express* **14,** 6308–6315 (2006).
12. Nozaki, K., Watanabe, H. & Baba, T. Photonic crystal nanolaser monolithically integrated with passive waveguide for effective light extraction. *Appl. Phys. Lett.* **92,** 021108 (2008).
13. Park, H. G. *et al.* Electrically driven single-cell photonic crystal laser. *Science* **305,** 1444–1447 (2004).
14. Park, H. G. *et al.* Characteristics of electrically driven two-dimensional photonic crystal lasers. *IEEE J. Quantum Electron.* **41,** 1131–1141 (2005).
15. Ellis, B. *et al.* Electrically pumped photonic crystal nanocavity light sources using a laterally doped p–i–n junction. *Appl. Phys. Lett.* **96,** 181103 (2010).
16. Long, C. M., Giannopoulos, A. V. & Choquette, K. D. Modified spontaneous emission from laterally injected photonic crystal emitter. *Elec. Lett.* **45,** 227–228 (2009).
17. Akahane, Y., Asano, T., Song, B. S. & Noda, S. High-*Q* photonic nanocavity in a two-dimensional photonic crystal. *Nature* **425,** 944–947 (2003).
18. Akahane, Y., Asano, T., Song, B. S. & Noda, S. Fine-tuned high-*Q* photonic-crystal nanocavity. *Opt. Express* **13,** 1202–1214 (2005).
19. Williams, C. C. Two-dimensional dopant profiling by scanning capacitance microscopy. *Ann. Rev. Mater. Sci.* **29,** 471–504 (1999).
20. Hill, M. *et al.* Lasing in metallic-coated nanocavities. *Nature Photon.* **1,** 589–594 (2007).
21. Reitzenstein, S. *et al.* Low threshold electrically pumped quantum dot–micropillar lasers. *Appl. Phys. Lett.* **93,** 061104 (2008).
22. Englund, D., Altug, H. & Vuckovic, J. Low-threshold surface-passivated photonic crystal nanocavity laser. *Appl. Phys. Lett.* **91,** 071124 (2007).
23. Vuckovic, J., Loncar, M., Mabuchi, H. & Scherer, A. Optimization of the *Q* factor in photonic crystal microcavities. *IEEE J. Quantum Electron.* **38,** 850–856 (2002).
24. Gong, Y. *et al.* Nanobeam photonic crystal cavity quantum dot laser. *Opt. Express* **18,** 8781–8789 (2010).
25. Nomura, M., Kumagai, N. Iwamoto, S., Ota, Y. & Arakawa, Y. Laser oscillation in a strongly coupled single-quantum-dot nanocavity system. *Nature Phys.* **6,** 279–283 (2010).

Acknowledgements

B.E. and G.S. were supported by the Stanford Graduate Fellowship. G.S. is also supported by the National Science Foundation graduate research fellowship program. The authors acknowledge support from the Interconnect Focus Center, the Air Force Office of Scientific Research Multidisciplinary Research Initiative for Complex and Robust On-chip Nanophotonics (G. Pomrenke; grant no. FA9550-09-1-0704), and the Director, Office of Science, Office of Basic Energy Sciences, Materials Sciences and Engineering Division, of the US Department of Energy (contract no. DE-AC02-05CH11231). The authors would like to thank I. Fushman for helpful discussions and M. Hilton of Veeco Instruments for advice regarding SCM. Work was performed in part at the Stanford Nanofabrication Facility of National Nanotechnology Infrastructure Network, supported by the National Science Foundation.

Author contributions

B.E. and J.V. designed the experiment and wrote the paper. T.S. and J.H. performed the molecular beam epitaxy growth of the samples. B.E. and M.M. fabricated the devices. B.E., M.M. and E.H. performed the fabricated laser material characterization. B.E. and G.S. performed electrical and optical measurements. B.E. analysed and modelled the data. All authors contributed to discussions.

Additional information

The authors declare no competing financial interests. Supplementary information accompanies this paper at www.nature.com/naturephotonics. Reprints and permission information is available online at http://www.nature.com/reprints/. Correspondence and requests for materials should be addressed to J.V.